RESEARCH ARTICLE Open Access

Light-driven molecular reorientation for large-scale photonic in-memory computing

Sijia Liu[1†], Xiaonan Hu[2,3†], Peng Chen[1*†], Xinyuan Fang[2,3*], Fangtianyu Chen[1], Kenong Li[1], Rui Sun[1], Shihui Ding[1], Yiheng Zhang[1], Keyao Li[2,3], Baoli Li[2,3], Shi-Jun Ge[1], Feng Wang[1], Min Gu[2,3*] and Yan-Qing Lu[1*]

Abstract

Photonics has the potential to transform high-speed and energy-efficient artificial intelligence. However, most photonic computing platforms still rely on costly electro-optic conversions for data input, weight loading and storage, resulting in substantial overhead during large-scale computation. Here, we present a large-scale photonic in-memory computing platform based on liquid crystal (LC)-enabled Poincaré-sphere-connected neural networks. Megabyte-level nonvolatile photonic memory is introduced through light-driven reorientation of sulfonic azo-dye and LC molecules, which also functions as the reconfigurable optical neurons. This architecture uniquely integrates optical sensing, memory, and computing in situ, allowing minimal data-movement overheads in various switchable machine vision tasks. Ultrahigh scalability is demonstrated by a 9.44-million-neuron photonic processor array that supports massively parallel optical computing, recording and retrieval, providing a memory capacity 100,000 times larger than state-of-the-art photonic in-memory computing. This work offers a novel pathway toward scalable submicrometer-precision photonic memory, thus establishing a new paradigm for physical neural networks and brain-like artificial intelligence.

Keywords Optical computing, Optical neural networks, Polarization optics, Liquid crystals, Reconfigurable microstructures

†Sijia Liu, Xiaonan Hu and Peng Chen have contributed equally to this work.

*Correspondence:
Peng Chen
chenpeng@nju.edu.cn
Xinyuan Fang
xinyuan.fang@usst.edu.cn
Min Gu
gumin@usst.edu.cn
Yan-Qing Lu
yqlu@nju.edu.cn
[1] National Laboratory of Solid State Microstructures, Key Laboratory of Intelligent Optical Sensing and Manipulation, College of Engineering and Applied Sciences, and Collaborative Innovation Center of Advanced Microstructures, Nanjing University, Nanjing 210093, China
[2] School of Artificial Intelligence Science and Technology, University of Shanghai for Science and Technology, Shanghai 200093, China
[3] Institute of Photonic Chips, University of Shanghai for Science and Technology, Shanghai 200093, China

1 Introduction

The rapid advancement of artificial intelligence (AI) is driving an urgent demand for more efficient computing architectures. Conventional von Neumann platforms, which separate memory and processing units, face fundamental limitations in speed and energy efficiency due to frequent data movement across electronic modules. Inspired by the seamless integration of sensing, memory, and computing in the human brain, emerging in-memory and in-sensor computing paradigms [1–4] seek to overcome this bottleneck by performing computation directly where data are stored or sensed, but remain limited by repeated digital-analog conversions, voltage-drop errors in crossbar wires, and device behaviour variations. Photonics, with ultralow latency and intrinsic parallelism, has emerged as another compelling alternative to overcome the von Neumann bottleneck [5, 6], facilitating high-throughput computation in both on-chip and free-space architectures. On-chip optical computing architectures based on Mach–Zehnder interferometers [7–10], optical attenuators [11], and micro-ring resonators [12, 13] offer advantages in compactness and computational density, whereas free-space architectures based on 3D-printed masks [14–16], spatial light modulators (SLMs) [17–19], and metasurfaces [20–23] excel in computational scale and parallelism. However, most current optical computing platforms are designed primarily as accelerators and still depend heavily on costly electro-optic conversions for data input, weight loading, and storage.

To approach brain-like efficiency and parallelism, it is essential to integrate optical sensing, memory, and computing in situ to minimize data movement. Recent advances in photonic in-memory computing [24] have demonstrated the potential for co-located storage and processing with either nonvolatile or volatile reconfigurability. Nonvolatile photonic in-memory chips have been developed for matrix multiplication based on phase-change materials [25–27] and magneto-optic materials [28]. Yet, their constrained spatial dimension and high optical loss intrinsically limit the interconnection scale of photonic networks. In contrast, free-space optical computing based on light diffraction [29] marks a milestone in scaling photonic neural networks. For in-memory matrix multiplication, weights can be directly encoded onto SLMs [30, 31] or tunable metasurfaces [32] in a volatile manner. For a wider range of applications, diffractive neural networks (DNNs) [14] have emerged as a compelling architecture, demonstrating remarkable success in image classification [33–35], optical imaging [36, 37], optical logic operation [38, 39], holographic reconstruction [40, 41], and wireless sensing [42]. However, these diffraction-based optical computing platforms either lack reconfigurability or rely on volatile electrical programming that requires continuous power supply. The absence of nonvolatile photonic memory poses a critical challenge to realizing large-scale photonic in-memory computing with minimal electro-optic conversion.

In this work, we present a scalable photonic in-memory computing platform using photo-rewritable liquid crystals (LCs). The LC molecules are programmed with iteratively trained in-plane orientations to construct Poincaré-sphere-connected vectorial DNNs, integrating high-dimensional optical computing with sensing capabilities. Via a polarization-sensitive dye, the LC orientations can be optically reconfigured to induce persistent trajectory variations on the interconnected Poincaré spheres, which further incorporates the nonvolatile photonic memory. In the experiment, up to 9.44 million reconfigurable vectorial neurons are built to support in-situ optical sensing, memory, and computing of vectorial light. Through expansion into large-scale processor arrays, this platform can achieve massively parallel computing, single-shot recording, and light-speed retrieval of 576 polarization encoding channels. It also allows flexible switching between various machine vision tasks while consuming negligible static power. This work greatly enhances the scalability and dimensionality of photonic in-memory computing, providing transformative opportunities for next-generation intelligent photonics and AI hardware.

2 Results

2.1 Photonic in-memory computing based on LC vectorial DNNs

As prototypical dynamic matter with strong anisotropy, LCs [43, 44] not only find wide applications in displays and SLMs, but can also convert the polarization of light [45–49], causing the evolution of states on the so-called Poincaré sphere—a prominent geometric representation of polarization [50]—according to their molecular arrangements. Here, using photo-rewritable LCs for nonvolatile photonic memory, we propose a new photonic in-memory computing platform based on Poincaré-sphere-connected vectorial DNNs as conceptually illustrated in Fig. 1a. For the input and output layers, the polarization of light at each position is described as a point on the Poincaré sphere. For the hidden layers, the vectorial neurons formed by space-variant polarization converters are described as numerous trajectories on the Poincaré spheres, with their start and end points indicating the polarization states before and after conversion. Through free-space diffraction of the vectorial light field, the Poincaré spheres in adjacent layers are interconnected across amplitude, phase, and polarization dimensions, thereby linking the input to the output vectorial light.

The nonvolatile photonic memory is developed through light-driven reorientation of LCs, leading to the Poincaré-sphere-reconfigurable DNN (Fig. 1b). For a given LC orientation, the corresponding polarization conversion trajectory on the Poincaré sphere is a circular arc rotating around a specific axis, whose angle with the S_1-axis is exactly twice the in-plane orientation angle of the LCs. The start point of the trajectory coincides with the incident polarization state, and its rotation angle equals the LC phase retardation (see Additional file 1: Note 1 for details). Intriguingly, by rewriting the LC orientation, this specific axis synchronously rotates, resulting in nonvolatile trajectory variations on the Poincaré sphere. Here, a photosensitive dye is utilized as the medium for the reorientation of LC molecules (Fig. 1c). When exposed to UV light with changing linear polarization, the photosensitive azo-dye molecules on substrates tend to reorient their absorption oscillators orthogonal to the UV polarization direction owing to their photoisomerization and

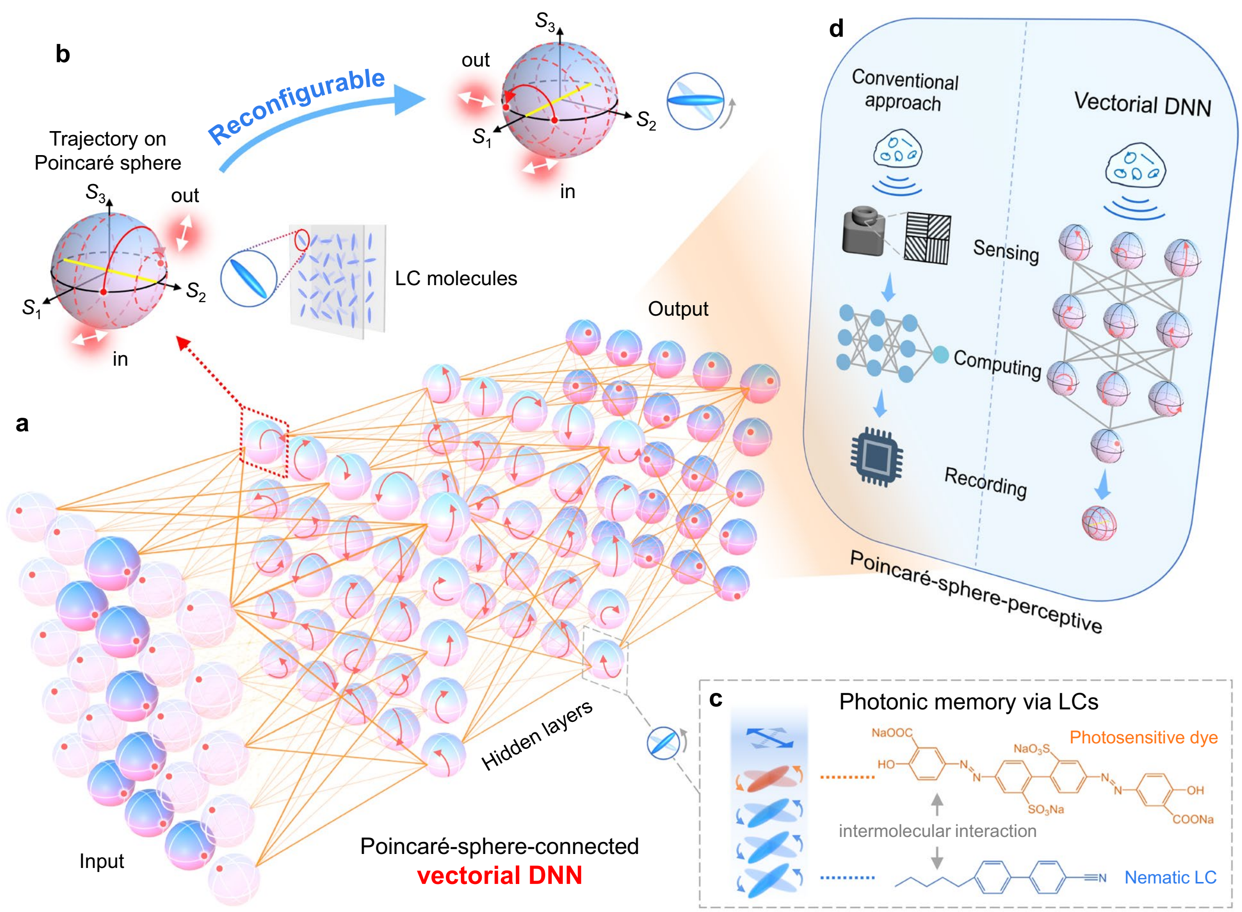

Fig. 1 Schematic of photonic in-memory computing based on LC vectorial DNNs. **a**, Schematic of the Poincaré-sphere-connected vectorial DNN. The points on the Poincaré spheres in the input and output layers represent local polarization states, and the arrows in the hidden layers represent various polarization conversions. The orange lines depict the diffraction-induced interconnections between adjacent layers. **b**, One of the LC-based reconfigurable Poincaré spheres in (**a**), showing that the trajectory (red arrow) on the Poincaré sphere can vary over time and act as nonvolatile photonic memory by rewriting the in-plane orientation of LC molecules (blue rods sandwiched by glass substrates). The white arrows indicate the polarization states before and after conversion. The red dashed circles around the switchable yellow axis (determined by the LC orientation) indicate other possible polarization conversions. **c**, Photonic memory mechanism of the LC-based Poincaré spheres, where nematic LC molecules tend to reorient orthogonal to the polarization of UV light in a nonvolatile manner due to the intermolecular interactions from photosensitive dye molecules. **d**, Potential application of the LC vectorial DNN in Poincaré-sphere-perceptive photonic in-memory computing. Compared to the conventional approach, where sensing, computing, and recording of polarized objects are performed in separate electronic modules, the vectorial DNN can complete all these processes in the same all-optical system

dichroic absorption. Through anisotropic intermolecular interactions, these azo-dye molecules will further reorient the adjacent LC molecules into the same alignment.

With large-scale reconfigurable Poincaré spheres, the LC vectorial DNN enables not only higher capacity and adaptability but also specialized functionalities such as Poincaré-sphere-perceptive photonic in-memory computing (Fig. 1d). Conventionally, sensing, computing, and recording of polarized objects are usually performed in separate electronic modules. In contrast, the vectorial DNN can simultaneously sense and distinguish them via the medium of light through proper manipulation of photonic memory in the Poincaré sphere array, and the computing results can be directly recorded in additional programmable Poincaré spheres, which holds great promise for real-time all-optical processing of ubiquitous light polarization.

2.2 In-situ optical computing via Poincaré-sphere-connected DNNs

To train the Poincaré-sphere-connected vectorial DNN to perform different tasks directly in the optical domain, we establish its forward propagation model using the Jones matrix method (Fig. 2a–c; Additional file 1: Fig. S1). As illustrated in Fig. 2a, each polarization state on the Poincaré sphere can be represented by a Jones vector

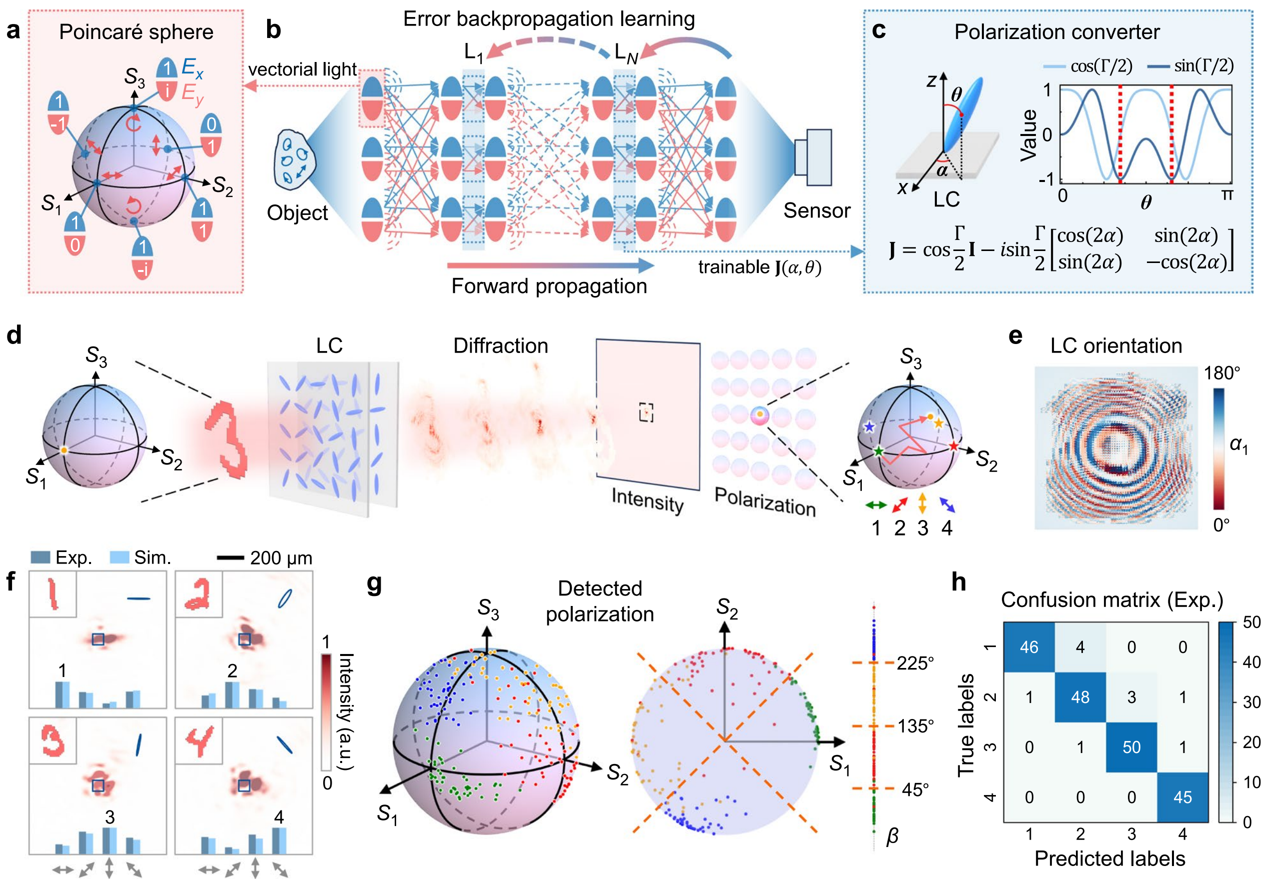

Fig. 2 Poincaré-sphere-connected DNN model for in-situ optical computing. **a**, Schematic of the Poincaré sphere. Six typical polarization states are marked on the sphere (red arrows) and labeled with their respective Jones vectors (unnormalized). **b**, Forward propagation and backpropagation model of the vectorial DNN. The independent diffraction of horizontally and vertically polarized light are depicted by blue and pink arrows, respectively. The arrows within blue dotted boxes indicate the trainable polarization conversion relations. **c**, Trainable Jones matrix **J** of LCs dependent on their tilt angle θ and in-plane orientation angle α. The red dotted lines in the θ-dependent curve chart mark the first-order half-wave condition of LCs. **d**, Schematic of intelligent polarization encoding, where different digits can be encoded into different polarization states (colourful stars and arrows) through diffraction. **e**, LC orientation distribution α_1 trained for the function in (**d**). **f**, Experimental results of digit classification via polarization encoding. The insets represent the input images. The intensity patterns are their respective output fields. The measured polarization ellipses (upper right) and polarization-filtered intensities (blue bars) indicate the averaged polarization within the detection area (blue square box). **g**, Detected polarization for 200 blind test images plotted in the 3D perspective (left), 2D top-down view (middle), and 1D equatorial projection (right) of the Poincaré sphere. The colours of the points indicate their respective true labels. β refers to the azimuthal angle of the Poincaré sphere. **h**, Experimental confusion matrix of the polarization encoding task

$\begin{bmatrix} E_x & E_y \end{bmatrix}^{\mathrm{T}}$. Consequently, the space-variant vectorial light field in the k-th layer can be vectorized as $\begin{bmatrix} \boldsymbol{E}_x^k & \boldsymbol{E}_y^k \end{bmatrix}^{\mathrm{T}}$, in which the 2D distributions of E_x and E_y are flattened into a column vector. Considering multiple layers of diffraction and modulation (Fig. 2b), the forward propagated vectorial light field can be formulated as

$$\begin{bmatrix} \boldsymbol{E}_x^{N+1} \\ \boldsymbol{E}_y^{N+1} \end{bmatrix} = \begin{bmatrix} \mathbf{W}^{N+1} & 0 \\ 0 & \mathbf{W}^{N+1} \end{bmatrix} \left(\prod_{k=N}^{1} \begin{bmatrix} \mathrm{diag}(\boldsymbol{J}_{xx}^k) & \mathrm{diag}(\boldsymbol{J}_{xy}^k) \\ \mathrm{diag}(\boldsymbol{J}_{yx}^k) & \mathrm{diag}(\boldsymbol{J}_{yy}^k) \end{bmatrix} \begin{bmatrix} \mathbf{W}^k & 0 \\ 0 & \mathbf{W}^k \end{bmatrix} \right) \begin{bmatrix} \boldsymbol{E}_x^0 \\ \boldsymbol{E}_y^0 \end{bmatrix}. \tag{1}$$

$\mathbf{W}^k$ denotes the diffractive weight matrix from the $(k-1)$-th layer to the k-th layer, which can be derived from the Rayleigh-Sommerfeld diffraction theory (see the Methods for more details). $\boldsymbol{J}_{xx}^k$, $\boldsymbol{J}_{xy}^k$, $\boldsymbol{J}_{yx}^k$, and $\boldsymbol{J}_{yy}^k$ represent the space-variant vectorial light modulations in the k-th layer, which are essentially the vectorized form of the 2×2 Jones matrix **J**. In this work, LCs serve as the polarization converters in the vectorial DNN (Fig. 2c). Their trainable Jones matrix $\mathbf{J}(\alpha, \theta)$ can be expressed as

$$\mathbf{J}(\alpha,\theta) = \cos\frac{\Gamma(\theta)}{2}\mathbf{I} - i\sin\frac{\Gamma(\theta)}{2}\begin{bmatrix}\cos(2\alpha) & \sin(2\alpha)\\ \sin(2\alpha) & -\cos(2\alpha)\end{bmatrix}, \tag{2}$$

where α and θ denote the in-plane orientation angle and out-of-plane tilt angle of the LCs, respectively; $\Gamma(\theta)$ represents the phase retardation; $\mathbf{I}$ is the identity matrix; and $i^2=-1$. For simplicity, LCs can be adjusted to a half-wave condition to keep $\cos(\Gamma/2)=0$ so that the Jones matrix depends solely on α. A loss function can be defined to quantify the difference between the output vectorial field and the ground truth (see Additional file 1: Note 2 for the definitions of different loss functions). Using the gradient-based error backpropagation algorithm, the α distribution in each LC layer can be iteratively updated to minimize the loss function, ultimately leading to the optimal parameters for the intended task.

As an explicit demonstration, we trained the Poincaré-sphere-connected DNN for intelligent polarization encoding, in which different images can be encoded into different polarization states. As shown in Fig. 2d, the handwritten digits 1 to 4 from the MNIST dataset are targeted to four separate points on the Poincaré sphere. Through the LC vectorial DNN, the input digit with horizontal polarization will gradually converge to the detection area (equivalently regarded as a single pixel), with its polarization state "walking" on the Poincaré sphere. On the basis of its final position relative to the four target points, the input digit can be rationally classified. In the experiment, the optimal orientation α_1 (Fig. 2e) was written into LCs through the first round of light-driven molecular reorientation. Some examples of its use in classifying 200 blind test handwritten digits are shown in Fig. 2f, in which the inference can be easily made by detecting the central polarization or by comparing the intensities under different analyser directions. Figure 2g presents the polarization encoding results for all 200 test images. From the 3D perspective, 2D top-down view, and 1D equatorial projection of the Poincaré sphere, different digits are clearly separated in the polarization space, leading to a high classification accuracy of 94.5% (Fig. 2h).

2.3 In-situ photonic memory for Poincaré-sphere-reconfigurable DNNs

The nonvolatile photonic memory via LCs was then explored to realize the Poincaré-sphere-reconfigurable DNN. In our dual-functional optical setup (Fig. 3a), blue and red lasers are used for LC reorientation and optical computing, respectively. By sandwiching an SLM between two achromatic quarter-wave plates, an arbitrary linear polarization distribution can be constructed for both lasers (see the Methods for details), which is then projected onto the LC device via a 4-f system. For the blue laser, this space-variant polarization can rewrite the vectorial DNN in a single shot, serving as the reconfigurable photonic memory. For the red laser, an additional polarizer is added in front of the LCs to convert the polarization distribution into an arbitrary amplitude image, which can directly serve as the input of the vectorial DNN. Compared with other micro/nano-polarization converters [51], the employed LC device requires only simple fabrication steps (Fig. 3b), offering a much more cost-effective and fabrication-friendly platform. Moreover, by setting the first diffraction distance to zero, memory rewriting and optical computing can even be conducted in situ without any movement of the LC device (Fig. 3c; see the Methods for details), completely avoiding any time-consuming light-to-device alignment. In this work, five different vectorial DNNs (α_1 to α_5) were successively reconfigured with the same LC device (Fig. 3d), verifying the remarkable optical reconfigurability of LC vectorial DNNs and their potential in photonic in-memory computing.

Leveraging this reconfigurability, we rewrote the vectorial DNN from α_1 to α_2 to achieve greater accuracy in polarization encoding through ensemble learning [52] (Fig. 3e). Since α_1 and α_2 were jointly trained (see Additional file 1: Note 3 and Fig. S2a for details), their joint inference can effectively correct some mispredictions from a single model (Fig. 3f), thereby enhancing the computing robustness. The joint confusion matrix for all 200 test images and its difference from the single-model matrices are shown in Fig. 3g,h, demonstrating an increased classification accuracy of 96.5% (see the simulation results in Additional file 1: Fig. S3). This ensemble learning of multiple sequential models suggests a new approach to achieving higher computing performance and supporting more complex tasks, which is as effective as adding spatial layers (Additional file 1: Fig. S2b-d).

2.4 In-situ polarized object sensing via Poincaré-sphere-perceptive DNNs

Furthermore, the LC orientation was reconfigured to α_3 (Fig. 3d) to demonstrate the Poincaré-sphere-perceptive DNN, which can simultaneously sense and compute polarization information. During training, nine categories of images in three polarization states were allocated to three detection areas (Fig. 4a) with a fixed horizontal analyser, enabling polarization-multiplexed classification and polarized object perception.

The three rows in Fig. 4a can be viewed as polarization multiplexing of three independent tasks (Additional file 1: Fig. S4a), including letter (E-MNIST), fashion item (Fashion-MNIST), and digit (MNIST) classifications. In

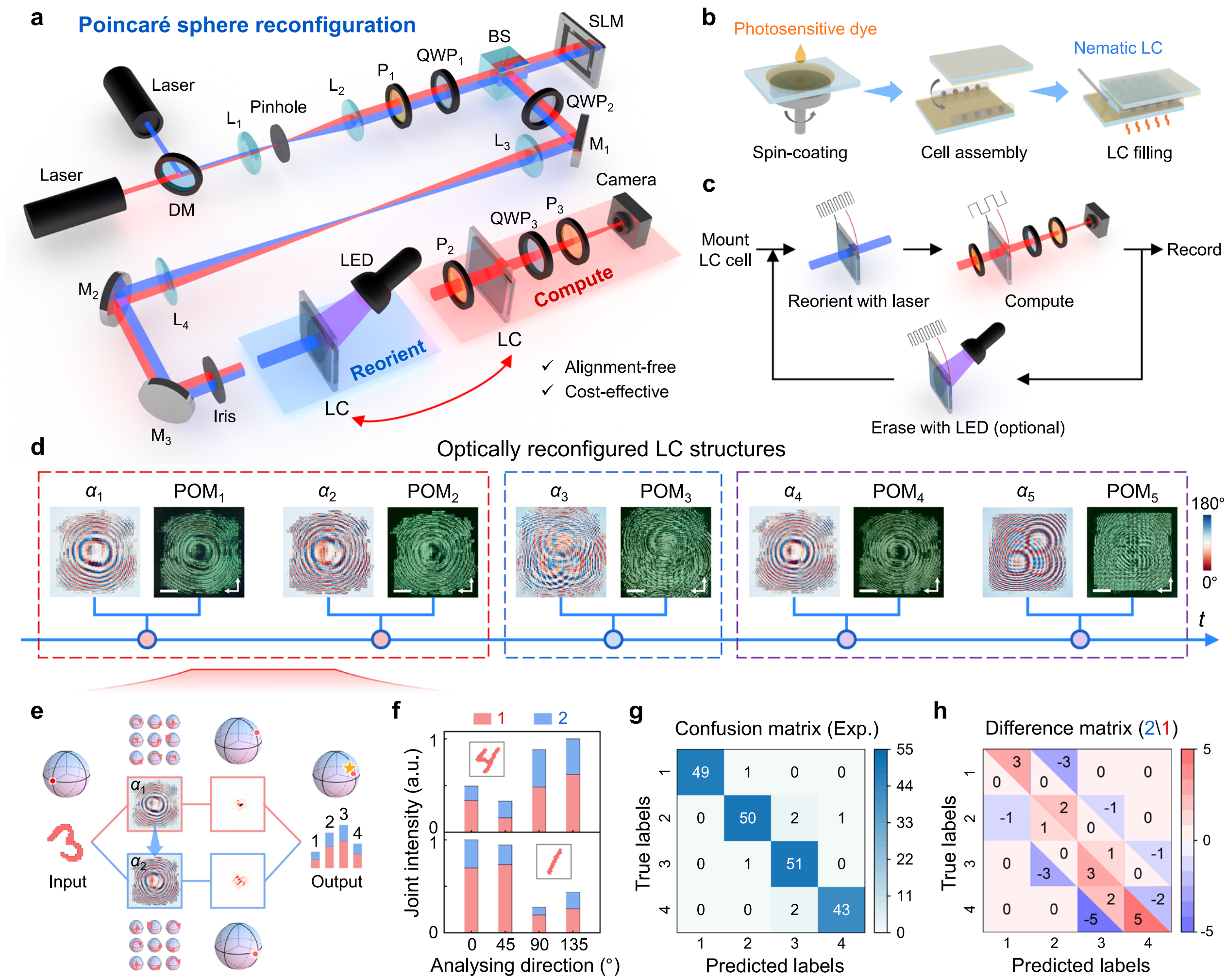

Fig. 3 Poincaré-sphere-reconfigurable DNN with in-situ photonic memory. **a**, Shared optical setup for LC reorientation and optical computing. DM, dichroic mirror; L_1-L_4, lenses; P_1-P_3, polarizers; QWP_1-QWP_3, quarter-wave plates; BS, beam splitter; SLM, spatial light modulator; M_1-M_3, mirrors; LED, light-emitting diode. The reorientation and computing modules can be switched in situ, leading to the nonvolatile photonic in-memory computing. **b**, Fabrication steps of the LC device. **c**, Repeatable memory rewriting process of the LC vectorial DNN. A high-frequency electrical signal (2 MHz) is applied during reorientation and erasing to improve the reconfiguration quality via the LC electrothermal effect. A low-frequency electrical signal (1 kHz) is applied during computing to satisfy the half-wave condition of LCs, which can be omitted with appropriate cell thickness. **d**, Five optically reconfigured LC structures involved in this work, including their trained LC orientation distributions (α_1-α_5) and respective polarized optical micrographs (POM_1-POM_5). The blue *t*-axis represents their reprogramming sequence. The red, blue and purple colours of the dashed rectangles and circles correspond to the three different functionalities involved in this work, namely polarization encoding, polarization perception, and optical recording. The white arrows depict the crossed polarizer and analyser. All scale bars represent 400 µm. **e**, Schematic of rewriting the vectorial DNN from α_1 to α_2 to make joint inference for digit classification, which is expected to enhance computing performance and robustness. **f**, Two examples of making joint inference by the two models. The insets represent the input images. Pink and blue bars represent the predictions from α_1 and α_2, respectively. **g**, Experimental confusion matrix based on the joint inference of α_1 and α_2. **h**, Difference matrix between (**g**) and single-model confusion matrices based solely on α_1 (upper right) or α_2 (lower left)

each polarization channel, the image category is determined by identifying the detection area with the highest intensity. Some experimental results are shown in Fig. 4b and Additional file 1: Fig. S4c, indicating that the input images with appropriate incident polarizations can be correctly classified. After 200 images were tested for each task, three polarization-dependent confusion matrices were obtained (Fig. 4c), with classification accuracies of 88%, 92.5%, and 93%. By adding a fully connected layer for adaptive training, these accuracies can be further improved to 91%, 95%, and 95.5% (Methods; Additional file 1: Fig. S5). Notably, while polarization significantly expands the computing capacity of DNNs, DNNs also help exceed the inherently limited number of polarization

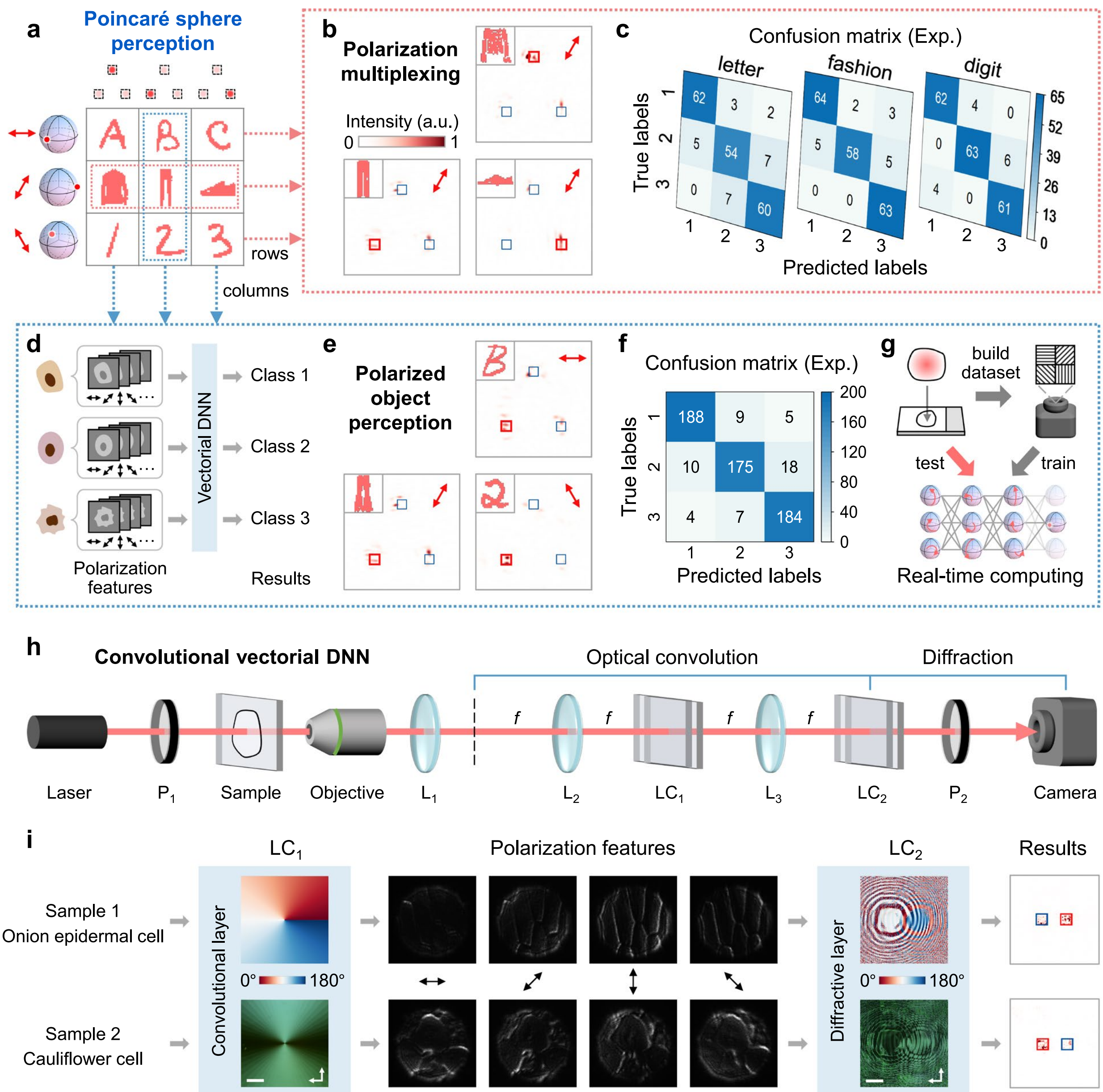

Fig. 4 Poincaré-sphere-perceptive DNN for in-situ polarized object sensing. **a**, Schematic of Poincaré-sphere-perceptive classification, where nine categories of images in three polarization states (red arrows and dots) are allocated to three detection areas with a fixed horizontal analyser. The three rows can be viewed as polarization multiplexing of three independent classification tasks, while the three columns can be viewed as the perception of three categories of polarized objects. **b**, Experimental results of polarization-multiplexed image classification in the second polarization channel. The insets represent the input images with their incident polarization marked by red arrows. The intensity patterns are their respective output fields. The detection areas with the highest overall intensities are highlighted by red square boxes, which indicate the predicted labels. **c**, Experimental confusion matrices of the three multiplexed image classification tasks. **d**, Schematic of polarized object perception, where objects with different polarization features can be sensed and classified by the vectorial DNN. **e**, Experimental results of polarized object perception for the second category. The insets conceptually represent different polarization features of the input polarized object, with their respective polarization marked by red arrows. **f**, Experimental confusion matrix of the polarized object perception task. **g**, Envisioned application of the vectorial DNN in real-time biological sample analysis and pathological diagnosis. **h**, Optical setup of the convolutional vectorial DNN for real-world cell classification. P_1-P_2, polarizers; L_1-L_3, lenses; LC_1-LC_2, photo-rewritable LC devices. The dashed line represents the imaging plane of the sample, which overlaps with the input plane of the 4-*f* system. **i**, Experimental results of sensing and classifying two types of plant cells. The scale bars in the micrographs represent 400 μm. The black arrows represent the polarization states of corresponding polarization features

channels (see the simulation results of 10-channel multiplexing in Additional file 1: Fig. S6).

More interestingly, the three columns in Fig. 4a can be viewed as the perception of three categories of polarized objects (Additional file 1: Fig. S4b), in which different images conceptually represent different polarization features of the input object. As illustrated in Fig. 4d, if all the polarization features can be correctly identified by the vectorial DNN, then their combination, i.e., the actual polarized object, can be reasonably classified. Experimentally, different polarization features belonging to the same object category tend to converge to the same detection area (Fig. 4e; Additional file 1: Fig. S4c), reaching a high classification accuracy of 91.2% for all 600 test polarization features (Fig. 4f). As an application example, this strategy is potentially applicable to real-time biological sample analysis and pathological diagnosis (Fig. 4g). After being trained with measured polarization features, the vectorial DNN can be used to classify tissue or cellular samples in an all-optical polarization-perceptive manner, thereby reducing computational latency and enhancing diagnostic accuracy.

In the proof-of-concept experiment, we constructed a novel convolutional vectorial DNN to directly sense and classify two types of plant cells, i.e., onion epidermal cells and cauliflower cells, in the optical domain. As shown in Fig. 4h, the convolutional vectorial DNN consists of a fixed optical convolutional layer and a trainable diffractive layer. The first LC device with a spiral-phase pattern is placed at the Fourier plane of a 4-*f* system to perform optical convolution, which can convert different edge directions into different polarization directions [46]. As a result, the onion epidermal cells with dominant vertical edges can produce a generally vertical polarization, whereas the cauliflower cells with multi-directional edges can produce a polarization with no preferred directions. The second LC device was trained using the polarization features of these cells after optical convolution and is placed at the output plane of the 4-*f* system to function as a polarization classifier. It can concentrate vertically polarized light and polarization-unbiased light into different detection areas, thereby enabling direct optical-domain classification of these two types of cells (see more details in Methods and Additional file 1: Fig. S7).

2.5 Large-scale photonic in-memory computing

Beyond weight storage in photonic in-memory computing, the nonvolatile photonic memory via LCs further suggests an ingenious way to incorporate single-shot vectorial light recording into DNNs. Because the photonic memory arises from the direct interaction between light and molecules, it can achieve a recording resolution down to the hundred-nanometer scale at sufficiently small layer thicknesses. As illustrated in Fig. 5a and Additional file 1: Fig. S8, the blue-light computing result of the vectorial DNN can be recorded by an additional LC device by reorienting LCs orthogonal to the output polarization. Similar to the memory rewriting process, the recorded light will activate the circles around a specific axis on the Poincaré sphere, which can be optically read or retrieved (see Additional file 1: Note 4 for details). To experimentally demonstrate this, we reconfigured the vectorial DNN to α_4 (Fig. 3d) to perform the same polarization encoding task as in Fig. 2d but for a blue-light wavelength. For an input digit “3”, this vectorial DNN generates a generally vertically polarized light spot (Fig. 5b) and thus horizontally reorients the LC molecules in the central area (Fig. 5c; see Additional file 1: Fig. S9 for more experimental results). A full-wave plate was inserted into the polarized optical microscope to read the recorded LC orientations (Fig. 5d; see Additional file 1: Fig. S10 for details), where the green colour verifies the horizontal LC orientation.

By integrating 12×12 vectorial DNN units with 9.44 million reconfigurable vectorial neurons (Fig. 5e; Additional file 1: Fig. S11), we further achieve large-scale photonic in-memory computing (Fig. 5f). Each identical unit in the array was trained to classify an input letter (“a”, “b”, “c”, or “d”) by encoding four light spots. Only the spot corresponding to the true label is optimized as vertically polarized, whereas the other three spots are optimized to be horizontally polarized, leading to 576 parallel polarization encoding channels in total. As an example, a 3×2 subarray was utilized to simultaneously classify the six letters “bad cab” (Fig. 5f (i)). With the optically reconfigured LC orientation α_5 (Fig. 5e), each letter can be encoded into four spots (Fig. 5f (ii)), with the spot corresponding to its true label optimized as vertically polarized. The output vectorial light can be recorded in another LC device and subsequently retrieved by laser illumination. Since the optical recording effect is weak at small exposure dosage below the threshold and tends to saturate at large exposure dosage, a sigmoid-shaped nonlinear relation naturally exists between the retrieved and recorded light (Fig. 5f (iii)), indicating its potential as a nonlinear activation function [53]. Such parallel optical recording is verified by the LC micrographs after recording (Fig. 5f (iv)), where 24 bright spots with positions and geometries consistent with the recorded light are observed. With an inserted full-wave plate, the categories of the six input letters can be inferred based on the observed colours. In general, the spots corresponding to the true labels appear closer to green, indicating the horizontal LC orientation and vertically polarized recorded light. Parallel optical retrieval is further achieved by illuminating the LC recording device with a laser. After

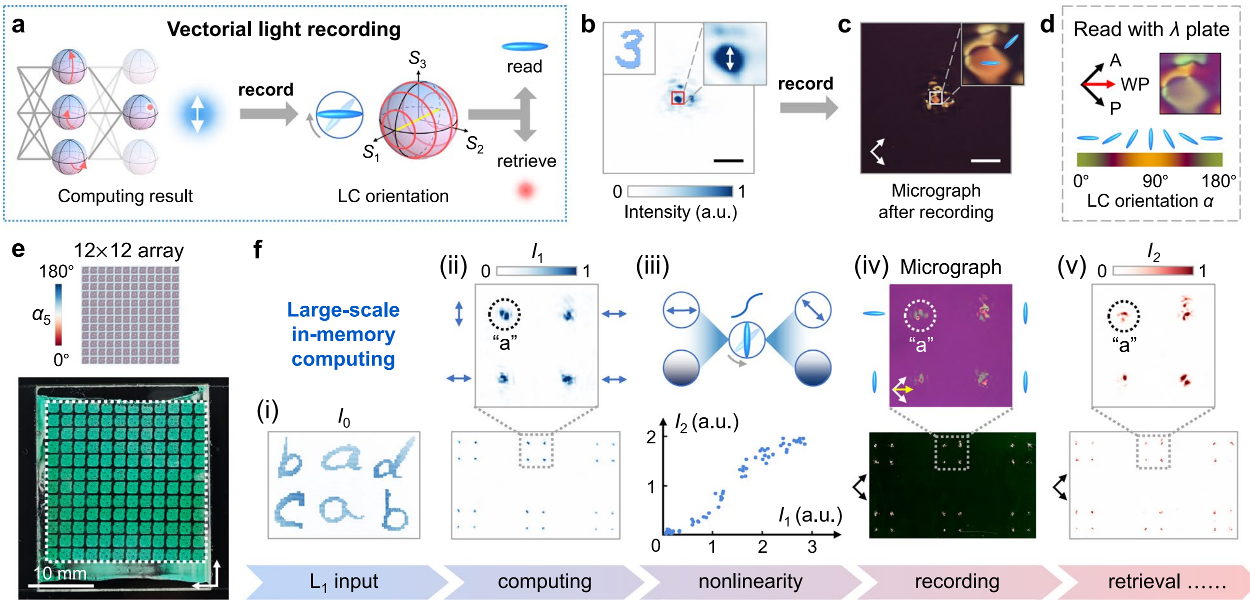

Fig. 5 Large-scale photonic in-memory computing. **a**, Schematic of vectorial light recording using the nonvolatile photonic memory via LCs. The white arrow represents the vertically polarized blue-light computing result, which can be recorded by reorienting LCs into horizontal alignment. The recorded information corresponds to the circles (red) around a specific axis (yellow) on the Poincaré sphere, which can be optically read or retrieved. **b**, Experimental computing result to be recorded in the blue-light polarization encoding task. The insets show the input image (upper left) and the enlarged intensity pattern marked with ideal polarization (upper right). **c**, Polarized micrograph of LCs after recording and the enlarged micrograph marked with ideal LC orientations (upper right). The white arrows depict the crossed polarizer and analyser. **d**, Readout of the LC orientation distribution with crossed polarizers (P and A) and a 530 nm full-wave plate (WP). The colour bar indicates the relation between colours and LC orientations. **e**, 12 × 12 large-scale array of the LC vectorial DNN α_5 (upper) and its real-world photo under crossed polarizers (lower). The effective area is enclosed by dotted lines. **f**, Experimental results of large-scale photonic in-memory computing based on the LC device in (**e**), including: (i) optical input example "bad cab"; (ii) output intensity pattern after parallel optical computing; (iii) nonlinear relation between retrieved and recorded light; (iv) micrographs of another LC device after recording the computing results, with black or white arrows labeling the crossed polarizers and the yellow arrow labeling the optional full-wave plate; (v) light-speed optical retrieval of the computing results under crossed polarizers, which can be used in the next all-optical loops. The experimental results for the second input letter "a" are enlarged and labeled with dotted circles, with the ideal output polarization and LC orientations marked in (ii) and (iv), respectively. The scale bars represent 200 μm in (**b**,**c**) and 10 mm in (**e**)

crossed polarizers, a light field containing the previously recorded computational results can be reconstructed at light speed (Fig. 5f (v)). This field can be further used in the next all-optical loops, enabling network extension, power regeneration, repeated data access, and temporal sequence processing in deep DNNs (Additional file 1: Fig. S8). More explanations and results can be found in Additional file 1: Note 5 and Fig. S12.

3 Discussions

By developing nonvolatile photonic memory compatible with large-scale free-space interconnections, the proposed platform substantially enhances the scalability of photonic in-memory computing, further enabling a brand-new class of memory-integrated free-space optical systems for end-to-end photonic processing, all-optical training, time-series computation, photonic switches, and photonic neuromorphic computing. Up to 9.44 million reconfigurable vectorial neurons with 8-bit weight precision are implemented to sense, compute, record, and retrieve vectorial light in a multi-core parallel manner, providing a high memory capacity of 151.04 Mbit across the two LC layers. Approximately 2.72×10^9 real-valued multiply-accumulate operations can be performed in memory at a time, which can lead to an effective computing speed of 5.44×10^{16} FLOPS, assuming real-world input and 10 MHz photodetectors are used. The task complexity is currently limited by a trade-off with high computational parallelism. By using large-scale neurons as a single-core processor, introducing additional diffractive layers (Additional file 1: Fig. S13), incorporating nonlinear activations (Additional file 1: Fig. S14), or constructing hybrid optoelectronic neural networks (Additional file 1: Fig. S15), more complex tasks can be solved with high performance. The memory rewriting speed highly depends on the power density and wavelength of the writing light. In our case, with a low-power continuous laser (450 nm, 2.05 mW/cm^2), the LC orientations can be rewritten within 60 s. This can be drastically shortened to below 100 ms by using a higher-power continuous laser (405 nm, 1.07×10^4 mW/cm^2) and potentially shortened to only 3 ns using an ultrahigh-peak-power femtosecond laser (400 nm, 1.24×10^{13} mW/cm^2) (Additional file 1: Fig. S16 and S17; Methods).

Compared to SLM-based solutions [30, 31] and the tunable metasurface solution from Neurophos [32], the proposed new platform is distinguished by its nonvolatile nature, which offers negligible driving power and high energy efficiency during static operation (Additional file 1: Table S1). It also offers a higher transmission efficiency of 92.5%, corresponding to an insertion loss as low as 0.34 dB, while its relatively limited rewriting speed makes it more suitable for problems that fit within the hardware resources and do not require external memory access. A more detailed performance assessment is provided in Additional file 1: Note 6 and Table S2, along with a comprehensive comparison with state-of-the-art optical computing technologies in Additional file 1: Tables S3 and S4. Moreover, this work demonstrates the unprecedented in-situ optical reconfiguration of vectorial light. By overcoming the intrinsic static constraint of conventional polarization platforms, it promises to transform polarization optics from a fixed-function paradigm into a programmable and adaptive one. This capability facilitates versatile polarization-related applications (see an envisioned deployable system for real-time biological sample analysis in Additional file 1: Fig. S18) and also suggests a pathway for sensing, computing, and recording of other dimensions of light [54], holding great potential for high-dimensional imaging [55–57], content generation [18, 58], and in situ training [59].

In summary, a large-scale photonic in-memory computing platform is developed based on light-driven reorientation of LC molecules. Its unique neural network architecture, depicted by an interconnected Poincaré sphere array, enables optical encoding, multiplexing, and perception of polarization information, substantially enhancing the dimensionality of current DNNs. The distinctiveness of the nonvolatile photonic memory further allows adaptable function switching, retrievable optical recording, and scalable parallel computing. This work establishes a new paradigm for optical neural networks by integrating optical sensing, memory, and computing in situ, opening new avenues for intelligent photonics and brain-like AI architectures.

4 Methods

4.1 Vectorial DNN model

In the forward propagation model of the vectorial DNN, the vectorial light fields in different layers are modulated by polarization converters and interconnected through free-space diffraction (Fig. 2a–c). For each position, the vectorial light field can be depicted by a Jones vector $\begin{bmatrix} E_x & E_y \end{bmatrix}^{\mathrm{T}}$. E_x and E_y refer to the horizontal and vertical polarization components, respectively. To describe the space-variant vectorial light field in the k-th layer of the vectorial DNN, the Jones vector can be further vectorized as $\begin{bmatrix} \boldsymbol{E}_x^k & \boldsymbol{E}_y^k \end{bmatrix}^{\mathrm{T}}$, where each element represents a polarization component within a single pixel. For example, a 256×256 area corresponds to a vectorized Jones vector with 131,072 elements (65,536 for each polarization component). If LCs are selected as the polarization converter, their modulation effects on vectorial light can be represented by a Jones matrix $\mathbf{J}$, which is dependent on the orientation angle α and the tilt angle θ of local LC molecules (Fig. 2c). The expression of $\mathbf{J}$ can be written as follows:

$$\begin{aligned}\mathbf{J} &= \mathbf{R}(-\alpha)\cdot\begin{bmatrix} \exp(-i\Gamma/2) & 0 \\ 0 & \exp(i\Gamma/2) \end{bmatrix}\cdot\mathbf{R}(\alpha) \\ &= \cos\frac{\Gamma}{2}\mathbf{I} - i\sin\frac{\Gamma}{2}\begin{bmatrix} \cos(2\alpha) & \sin(2\alpha) \\ \sin(2\alpha) & -\cos(2\alpha) \end{bmatrix}\end{aligned}. \quad (3)$$

$\mathbf{R}$ is the rotation matrix, $\mathbf{I}$ is the identity matrix, and $i^2=-1$. Γ is the phase retardation resulting from the birefringence of LCs, which can be expressed as

$$\Gamma = \frac{2\pi(n_{\mathrm{eff}} - n_{\mathrm{o}})d}{\lambda}, \quad (4)$$

where d is the thickness of the LC layer, λ is the wavelength of incident light, n_{o} is the ordinary refractive index, and n_{eff} is the effective extraordinary refractive index dependent on θ. For simplicity, n_{eff} or d can be adjusted to keep $\cos(\Gamma/2)=0$ and $\sin(\Gamma/2)=-1$ (i.e., the half-wave condition), so the Jones matrix becomes

$$\mathbf{J}' = \begin{bmatrix} J_{xx} & J_{xy} \\ J_{yx} & J_{yy} \end{bmatrix} = i\begin{bmatrix} \cos(2\alpha) & \sin(2\alpha) \\ \sin(2\alpha) & -\cos(2\alpha) \end{bmatrix}, \quad (5)$$

which is solely dependent on the optically reconfigurable parameter α. Similar to E_x and E_y, the four elements of $\mathbf{J}'$ (i.e., J_{xx}, J_{xy}, J_{yx}, and J_{yy}) can also be vectorized to represent the spatial variance of vectorial light modulation. Accordingly, the transform of the vectorial light field between successive layers can be formulated as

$$\begin{bmatrix} \boldsymbol{E}_x^k \\ \boldsymbol{E}_y^k \end{bmatrix} = \begin{bmatrix} \mathrm{diag}(\boldsymbol{J}_{xx}^k) & \mathrm{diag}(\boldsymbol{J}_{xy}^k) \\ \mathrm{diag}(\boldsymbol{J}_{yx}^k) & \mathrm{diag}(\boldsymbol{J}_{yy}^k) \end{bmatrix}\begin{bmatrix} \mathbf{W}^k & 0 \\ 0 & \mathbf{W}^k \end{bmatrix}\begin{bmatrix} \boldsymbol{E}_x^{k-1} \\ \boldsymbol{E}_y^{k-1} \end{bmatrix}, \quad (6)$$

where $\mathbf{W}^k$ denotes the diffractive weight matrix from the (k – 1)-th to the k-th layer; $\boldsymbol{J}_{xx}^k$, $\boldsymbol{J}_{xy}^k$, $\boldsymbol{J}_{yx}^k$, and $\boldsymbol{J}_{yy}^k$ represent the vectorial light modulation in the k-th layer, which are essentially the vectorized form of the four elements in the Jones matrix $\mathbf{J}'$. Considering multiple layers of diffraction and modulation, the forward propagated vectorial light field can be formulated as

$$\begin{bmatrix} \boldsymbol{E}_x^{N+1} \\ \boldsymbol{E}_y^{N+1} \end{bmatrix} = \begin{bmatrix} \mathbf{W}^{N+1} & 0 \\ 0 & \mathbf{W}^{N+1} \end{bmatrix} \left(\prod_{k=N}^{1} \begin{bmatrix} \mathrm{diag}(\boldsymbol{J}_{xx}^k) & \mathrm{diag}(\boldsymbol{J}_{xy}^k) \\ \mathrm{diag}(\boldsymbol{J}_{yx}^k) & \mathrm{diag}(\boldsymbol{J}_{yy}^k) \end{bmatrix} \begin{bmatrix} \mathbf{W}^k & 0 \\ 0 & \mathbf{W}^k \end{bmatrix} \right) \begin{bmatrix} \boldsymbol{E}_x^0 \\ \boldsymbol{E}_y^0 \end{bmatrix}. \tag{7}$$

The diffraction in DNNs is usually explained by the Rayleigh-Sommerfeld diffraction theory, which considers each neuron as a secondary wave source. Assuming the position of the secondary wave source is (x_m, y_m, z_m), the complex-valued diffractive weighting function that represents the contribution of this source to the m'-th neuron of the k-th layer at (x, y, z) can be expressed as

$$w_{m'}^k(x, y, z) = \frac{z - z_m}{r^2} \left(\frac{1}{2\pi r} + \frac{1}{i\lambda} \right) \exp\left(\frac{i2\pi r}{\lambda} \right), \tag{8}$$

where λ is the wavelength and i is the imaginary unit. r can be expressed as

$$r = \sqrt{(x - x_m)^2 + (y - y_m)^2 + (z - z_m)^2}. \tag{9}$$

According to Eq. (8), light diffraction is a linear process that can connect the output from the previous layer to a broad region in the following layer.

In this work, the angular spectrum method was used for higher computational efficiency. The angular spectrum method can calculate the diffraction result by two Fourier transforms, which is equivalent to the convolutional form of Rayleigh-Sommerfeld diffraction. The propagation of vectorial light is regarded as the independent propagation of two orthogonal polarization components, such as E_x and E_y. Their diffraction processes for a distance d have the same expression as follows:

$$E_s(x, y, d) = \mathcal{F}^{-1}\{\mathcal{F}[E_s(x, y, 0)] \times H(f_x, f_y, d)\}, \tag{10}$$

where E_s can be E_x or E_y, $\mathcal{F}$ ($\mathcal{F}^{-1}$) is the two-dimensional Fourier (inverse Fourier) transform operator, and H is the transfer function of free-space diffraction. (x, y) and (f_x, f_y) represent spatial coordinates and spatial frequency coordinates, respectively. The expression of H is as follows:

$$H(f_x, f_y, d) = \exp\left(i\frac{2\pi}{\lambda} d \sqrt{1 - (\lambda f_x)^2 - (\lambda f_y)^2} \right). \tag{11}$$

Besides, the polarization detection process can optionally be incorporated into the forward propagation model of vectorial DNNs, through multiplying the output vectorial light field by the Jones matrices of polarizers. The intensities filtered out at different polarization directions can be variously designed as the criterions for inference.

4.2 Model training

In our model, LCs function as the reconfigurable vectorial neurons to program the interconnected Poincaré spheres in the neural network, so we set the LC orientation distribution α as the trainable parameter. The size for a single vectorial DNN unit was set to be 256×256 for an area of 4.19 mm^2. The diffraction distance was selected as 10 cm for satisfactory computing performance. For the different functions reported in this work, various loss functions were defined to quantify the difference between the output vectorial light field and the ground truth (see definitions of all these loss functions in Additional file 1: Notes 2 and 3). Then, the error backpropagation learning was implemented using Python 3.9.13 and TensorFlow 2.12.0 on a server (Nvidia RTX 4090 24 GB GPU, Intel Xeon Gold 6226R CPU, 256 GB of RAM and the Microsoft Windows 11 operating system), in order to find the optimal LC orientation distribution that can minimize the loss function. The training and test images of handwritten digits, fashion items, and letters used in this work are sourced from the MNIST, Fashion-MNIST, and E-MNIST datasets, respectively.

Regarding the training of the convolutional vectorial DNN, the LC convolutional layer is fixed as a 768×768 spiral-phase pattern, and only the 256×256 LC diffractive layer needs to be trained. Instead of employing both intensity patterns and polarization states for training, the training process of the diffractive layer leverages only the averaged polarization states of the optical convolution results, which simplifies the training process and allows the diffractive layer to function as a robust polarization classifier.

Regarding the electrical adaptive training, shallow fully connected layers can be added to compensate for the system errors and thus improve the experimental performance. For each task of the polarization-multiplexed image classification, a single fully connected layer with 12 learnable parameters was added, along with the Softmax nonlinear activation function (Additional file 1: Fig. S5c). These parameters were trained based on experimental results, which were obtained through the optical classification of 500 training images. In this hybrid optoelectronic neural network, the electronic part accounts for only 0.05% of the total trainable parameters, but increases the experimental test accuracies by 2.5–3%.

4.3 Device fabrication and reconfiguration

The two key materials involved in this work are the photosensitive sulfonic azo-dye SD1 (DIC, Japan) and the nematic LC 5CB (HCCH, China), with their chemical structures shown in Fig. 1c. The major fabrication steps of the LC device are illustrated in Fig. 3b. First, the solid-state SD1 was dissolved in dimethylformamide at a concentration of 0.35 wt.%. Next, two indium-tin-oxide (ITO) glass substrates were UV-Ozone treated and then spin-coated with this SD1 solution. After curing at 100 °C for 10 min, these two substrates were assembled into an empty cell with 7-μm spacer/glue mixtures in between. Afterwards, this cell was heated to 55 °C and then filled with 5CB (clearing point: 35 °C) via the capillary action.

After cooling to the room temperature, the fabricated LC device can be mounted in the optical setup (Fig. 3a) to perform repeatable memory rewriting and in-memory computing. Thanks to the shared optical setup for LC reorientation and optical computing, the LC vectorial DNN can be optically reconfigured in situ without any movement of the LC device, acting as the nonvolatile photonic memory. Specifically, when exposed to linearly polarized UV light, SD1 molecules tend to align orthogonally to the local polarization direction. Via the intermolecular interactions between SD1 and 5CB molecules, 5CB can acquire the same orientation distribution as SD1. Notably, blue light also falls within the absorption spectrum of SD1, allowing light-driven reorientation of LCs. In this work, the arbitrary linear polarization distribution was created by the SLM-based polarization projection system (specified in Experimental Setup, Methods). Up to 2.07 million vectorial neurons (1920×1080) can be optically reconfigured at once using the SLM, which can be further scaled up (almost infinitely in theory) by translating the LC device for tiling operations. During each optical reconfiguration process, a 365 nm light-emitting diode (LED; 42.5 mW/cm^2, 10 s) was used to erase the original LC orientations, which can accelerate the subsequent rewriting process, and a 450 nm laser (2.05 mW/cm^2, 60 s) was used to rewrite new orientations (Fig. 3c). To improve the rewriting quality, a 2 MHz, 10 V square wave was applied during erasing and reorientation to transform LCs into the isotropic phase via the electrothermal effect, which can be omitted when the full-wave condition is satisfied. Notably, the 450 nm laser used here is a low-power source and does not perfectly match the absorption peak of SD1. After testing the optical reconfigurability of LCs using a higher-power continuous laser (405 nm, 1.07×10^4 mW/cm^2) and an ultrahigh-peak-power femtosecond laser (400 nm, 1.24×10^{13} mW/cm^2), we find that even in the absence of LED erasing, the laser rewriting time can be drastically reduced to 100 ms and 3 ns, respectively (Additional file 1: Fig. S16 and S17).

4.4 Experimental setup

As shown in Fig. 3a, the reported memory rewriting and optical computing were conducted in the same optical setup. A blue laser (450 nm) and a red laser (632.8 nm) are combined and then expanded by a factor of 16.67, used as reorientation and computing light, respectively. A polarizer is followed to convert both lasers into linear polarization. After the polarizer, a reflective SLM (PLUTO-2.1-NIR-145, Holoeye Photonics AG, Germany; resolution: 1920×1080, pixel pitch: 8 μm) is sandwiched between two achromatic quarter-wave plates (AWP20Q-T2Q, JCOPTIX, China), which can construct arbitrary linear polarization distribution for both lasers. The underlying principle is that the first quarter-wave plate can convert the lasers into circularly polarized light, with equal-intensity horizontal and vertical polarization components. The SLM can only program the phase of the horizontal polarization component, while directly reflecting the vertical polarization component without any modulation. The second quarter-wave plate can transform these two linear polarization components into two orthogonal circular polarization components, with one circular polarization modulated and the other not. According to the phase difference between these two components, which is arbitrarily controlled by the SLM, the linear polarization direction of their superposition can be arbitrarily determined.

The generated polarization distribution is then projected onto the LC device via a 4-*f* imaging system composed of two achromatic lenses (OLD2466-T2, JCOPTIX, China). Using the blue laser, LC orientations can be rewritten by the space-variant polarization with the aid of a UV LED, achieving the optical reconfiguration of the photonic memory. When performing optical computing with the red laser, the same optical setup is used with several additional polarizing and analysing elements. The polarizer added in front of the LCs can convert the generated polarization distribution into an arbitrary amplitude image, which can directly serve as the input of the vectorial DNN. Notably, the uniform polarization direction of the amplitude image can also be customized, yielding the differently polarized input for the Poincaré-sphere-perceptive classification tasks. A uniform voltage (1 kHz, ~ 1 V) is applied to LCs during computing to satisfy their half-wave condition, which is theoretically dispensable with appropriate cell thickness. The quarter-wave plate, polarizer and camera behind the LCs are used to detect the vectorial light fields at the output plane, namely, the computing results. This part can be replaced by other vectorial light sensors, such as polarization detectors or another LC device as shown in Fig. 5a. In this work, the alignment-free LC reorientation and optical computing were achieved by setting the first diffraction distance to zero in the forward propagation model. In other cases, the light-to-device alignment process can also be substantially simplified by using a translation stage to move the LC device precisely along the optical axis.

In the experimental setup for the convolutional vectorial DNN (Fig. 4h), a 20× objective and a lens are used for the magnified imaging of plant cell samples. The corresponding imaging plane overlaps with the front focal plane of a 4-*f* system, which can perform two optical Fourier transforms. The first LC device is placed at the Fourier plane of the 4-*f* system to perform optical convolution, while the second LC device is placed at the back focal plane of the 4-*f* system to function as a polarization classifier. Using this optical setup, the onion epidermal cells and cauliflower cells can be easily classified by identifying the overall output intensities within the two predefined detection areas.

4.5 Characterizations

All the micrographs were captured using a polarized optical microscope (Ci-POL, Nikon, Japan) under the transmission mode. Brightness variation in the micrographs was observed under the crossed polarizer and analyser, and colour variation which better reflects the LC orientations was observed with an additional 530 nm full-wave plate (45° to the crossed polarizers). The output light fields of the convolutional vectorial DNN were measured by a polarization camera (CS505MUP1, Thorlabs, USA). All the other intensity distributions were recorded by a colour CMOS camera (CS165CU, Thorlabs, USA). To characterize the polarization of the output vectorial light, we measured the intensities of six different polarization components ($I_{0°}$, $I_{45°}$, $I_{90°}$, $I_{135°}$, I_{left}, I_{right}) using the combination of a quarter-wave plate and a polarizer. The overall intensity within each detection area was obtained by matching the measured intensity pattern to the predefined detection areas through an initial calibration step and then summing the pixel values within each area. Afterwards, the Stokes parameters S_1, S_2, and S_3 of the output vectorial light were calculated through the following expressions:

$$\begin{cases} S_1 = I_{0^\circ} - I_{90^\circ} \\ S_2 = I_{45^\circ} - I_{135^\circ} \\ S_3 = I_{\text{left}} - I_{\text{right}} \end{cases}. \tag{12}$$

After normalization, these three parameters became the coordinates of a point on the Poincaré sphere, offering a prominent geometric representation of the output polarization state. Besides, the power density of the erasing light and the reorientation light were measured by a digital optical power meter (PM100D, Thorlabs, USA). The minimum exposure time for memory rewriting was determined by varying the exposure time and then evaluating the corresponding LC reorientation quality by calculating the coefficient of variation within the reorientation area of the polarized optical micrograph (Additional file 1: Fig. S16 and S17).

Supplementary Information

The online version contains supplementary material available at https://doi.org/10.1186/s43593-026-00141-0.

Additional file 1 (PDF 6107 KB)

Acknowledgements

This work was supported by the National Key R&D Program of China (Nos. 2021YFA1202000, and 2022YFA1203700), the National Natural Science Foundation of China (NSFC) (Nos. T2488302, 62222507, 62422509, 62575180, and 624B2065), the Shanghai Natural Science Foundation (No. 25ZR1402386), the Natural Science Foundation of Jiangsu Province (No. BK20243067), the Shanghai Science and Technology Innovation Action Plan (No. 25LN3201000), Shanghai Municipal Education Commission (23SG41), the Shanghai Municipal Science and Technology Major Project, and the Fundamental Research Funds for the Central Universities (No. 0213-14380292). We acknowledge Prof. W. Chen and Dr. A. Yu for their help with the femtosecond laser experiment.

Author contributions

S.L., P.C., X.F., M.G., and Y.L. conceived the original idea. S.L., X.H., P.C., X.F., M.G., and Y.L. designed the experiment. S.L. and X.H. conducted the numerical simulations, fabricated the samples, and performed the experiments with the assistance of P.C., X.F., F.C., K.L., R.S., S.D., Y.Z., K.L., B.L., S.G., and F.W.. S.L., X.H., P.C., and X.F. analysed the data and prepared the initial manuscript. All authors participated in the discussion, and contributed to refining the manuscript. P.C., X.F., M.G., and Y.L. co-supervised and directed the research.

Availability of data and materials

All data supporting this study and its findings are available within this article and its Supplementary Information. Any other relevant data are available from the corresponding authors upon request.

Declarations

Competing interests

Min Gu serves as an Editor for the Journal, no other author has reported any competing interests.

Received: 6 February 2026 Revised: 30 July 2026 Accepted: 5 August 2026
Published online: 31 August 2026

References

1. D. Ielmini, H.-S.P. Wong, In-memory computing with resistive switching devices. Nat. Electron. **1**, 333–343 (2018)
2. A. Sebastian, M. Le Gallo, R. Khaddam-Aljameh, E. Eleftheriou, Memory devices and applications for in-memory computing. Nat. Nanotechnol. **15**, 529–544 (2020)
3. F. Zhou, Y. Chai, Near-sensor and in-sensor computing. Nat. Electron. **3**, 664–671 (2020)
4. T. Wan, B. Shao, S. Ma et al., In-sensor computing: materials, devices, and integration technologies. Adv. Mater. **35**, 2203830 (2023)

5. N.H. Farhat, D. Psaltis, A. Prata, E. Paek, Optical implementation of the Hopfield model. Appl. Opt. **24**, 1469–1475 (1985)
6. D. Psaltis, D. Brady, X.-G. Gu, S. Lin, Holography in artificial neural networks. Nature **343**, 325–330 (1990)
7. Y. Shen, N.C. Harris, S. Skirlo et al., Deep learning with coherent nanophotonic circuits. Nat. Photonics **11**, 441–446 (2017)
8. Z. Xu, T. Zhou, M. Ma et al., Large-scale photonic chiplet Taichi empowers 160-TOPS/W artificial general intelligence. Science **384**, 202–209 (2024)
9. S. Hua, E. Divita, S. Yu et al., An integrated large-scale photonic accelerator with ultralow latency. Nature **640**, 361–367 (2025)
10. X. Yu, Z. Wei, F. Sha et al., Parallel optical computing capable of 100-wavelength multiplexing. eLight **5**, 10 (2025)
11. F. Ashtiani, A.J. Geers, F. Aflatouni, An on-chip photonic deep neural network for image classification. Nature **606**, 501–506 (2022)
12. J. Feldmann, N. Youngblood, C.D. Wright, H. Bhaskaran, W.H.P. Pernice, All-optical spiking neurosynaptic networks with self-learning capabilities. Nature **569**, 208–214 (2019)
13. Y. Wang, K. Liao, K. Zhang et al., Reconfigurable versatile integrated photonic computing chip. eLight **5**, 20 (2025)
14. X. Lin, Y. Rivenson, N.T. Yardimci et al., All-optical machine learning using diffractive deep neural networks. Science **361**, 1004–1008 (2018)
15. C.-Y. Shen, J. Li, Y. Li et al., Multiplane quantitative phase imaging using a wavelength-multiplexed diffractive optical processor. Adv. Photonics **6**, 056003 (2024)
16. J. Hu, K. Liao, N.U. Dinç et al., Subwavelength imaging using a solid-immersion diffractive optical processor. eLight **4**, 8 (2024)
17. T. Zhou, X. Lin, J. Wu et al., Large-scale neuromorphic optoelectronic computing with a reconfigurable diffractive processing unit. Nat. Photonics **15**, 367–373 (2021)
18. S. Chen, Y. Li, Y. Wang, H. Chen, A. Ozcan, Optical generative models. Nature **644**, 903–911 (2025)
19. Y. Zhang, X. Liu, C. Yang et al., Direct tensor processing with coherent light. Nat. Photonics **20**, 102–108 (2026)
20. C. Liu, Q. Ma, Z.J. Luo et al., A programmable diffractive deep neural network based on a digital-coding metasurface array. Nat. Electron. **5**, 113–122 (2022)
21. M. Luo, M. Jiang, B.J. Shastri et al., Highly scalable machine vision enabled with meta-optics-based ultra-wide neural network. eLight **6**, 10 (2026)
22. N. Wu, Y. Sun, J. Hu et al., Intelligent nanophotonics: when machine learning sheds light. eLight **5**, 5 (2025)
23. X. Luo, Y. Hu, X. Ou et al., Metasurface-enabled on-chip multiplexed diffractive neural networks in the visible. Light Sci. Appl. **11**, 158 (2022)
24. C. Ríos, N. Youngblood, Z. Cheng et al., In-memory computing on a photonic platform. Sci. Adv. **5**, eaau5759 (2019)
25. J. Feldmann, N. Youngblood, M. Karpov et al., Parallel convolutional processing using an integrated photonic tensor core. Nature **589**, 52–58 (2021)
26. B. Dong, S. Aggarwal, W. Zhou et al., Higher-dimensional processing using a photonic tensor core with continuous-time data. Nat. Photonics **17**, 1080–1088 (2023)
27. W. Zhou, B. Dong, N. Farmakidis et al., In-memory photonic dot-product engine with electrically programmable weight banks. Nat. Commun. **14**, 2887 (2023)
28. P. Pintus, M. Dumont, V. Shah et al., Integrated non-reciprocal magneto-optics with ultra-high endurance for photonic in-memory computing. Nat. Photonics **19**, 54–62 (2025)
29. J. Hu, D. Mengu, D.C. Tzarouchis et al., Diffractive optical computing in free space. Nat. Commun. **15**, 1525 (2024)
30. Y. Liang, J. Wang, K. Xue et al., High-clockrate free-space optical in-memory computing. Light Sci. Appl. **15**, 115 (2026)
31. M.H. Latifpour, B.J. Park, Y. Yamamoto, M.-G. Suh, Hyperspectral in-memory computing with optical frequency combs and programmable optical memories. Optica **11**, 932–939 (2024)
32. M. Shebanow, H. Finkelstein, P. Bowen, Revolutionizing the AI data center: Delivering 4,000 peta operations per second at 1% of the power using optical systolic arrays. Neurophos Inc. (2025). https://11549dc2-0dc9-4363-9a47-d257d2a497cc.filesusr.com/ugd/79aa3c_85cd1a5477d44f4fa0e423c03ad0746c.pdf?index=true
33. X. Fang, X. Hu, B. Li et al., Orbital angular momentum-mediated machine learning for high-accuracy mode-feature encoding. Light Sci. Appl. **13**, 49 (2024)
34. Y. Dong, Y. Bai, Q. Zhang, H. Luan, M. Gu, High-throughput optical neuromorphic graphic processing at millions of images per second. eLight **5**, 29 (2025)
35. M. Liu, X. Ye, Y. Zhou, D. Tang, F. Fan, Polarization-multiplexed diffractive neural networks for multi-task classification based on liquid crystals. Opt. Lett. **50**, 5446–5449 (2025)
36. H. Yu, Z. Huang, S. Lamon et al., All-optical image transportation through a multimode fibre using a miniaturized diffractive neural network on the distal facet. Nat. Photonics **19**, 486–493 (2025)
37. Z. Guo, Z. Tan, X. Zang et al., Polarization-selective unidirectional and bidirectional diffractive neural networks for information security and sharing. Nat. Commun. **16**, 4492 (2025)
38. C. Qian, X. Lin, X. Lin et al., Performing optical logic operations by a diffractive neural network. Light Sci. Appl. **9**, 59 (2020)
39. X. Ding, Z. Zhao, P. Xie et al., Metasurface-based optical logic operators driven by diffractive neural networks. Adv. Mater. **36**, 2308993 (2024)
40. Z. Fan, C. Qian, Y. Jia et al., Holographic multiplexing metasurface with twisted diffractive neural network. Nat. Commun. **15**, 9416 (2024)
41. J. Wang, J. Chen, F. Yu et al., Unlocking ultra-high holographic information capacity through nonorthogonal polarization multiplexing. Nat. Commun. **15**, 6284 (2024)
42. S. Gao, H. Chen, Y. Wang et al., Super-resolution diffractive neural network for all-optical direction of arrival estimation beyond diffraction limits. Light Sci. Appl. **13**, 161 (2024)
43. D. Andrienko, Introduction to liquid crystals. J. Mol. Liq. **267**, 520–541 (2018)
44. P. Chen, B.Y. Wei, W. Hu, Y.Q. Lu, Liquid-crystal-mediated geometric phase: from transmissive to broadband reflective planar optics. Adv. Mater. **32**, 1903665 (2020)
45. L. Zhou, T. Zhong, Y. Liu et al., When structured light encounters liquid crystals. Adv. Funct. Mater. **34**, 2404614 (2024)
46. W. Chen, D. Zhu, S.-J. Liu et al., Fast selective edge-enhanced imaging with topological chiral lamellar superstructures. Natl. Sci. Rev. **11**, nwae247 (2024)
47. Y.H. Zhang, S.J. Liu, P. Chen et al., Logical rotation of non-separable states via uniformly self-assembled chiral superstructures. Nat. Commun. **15**, 1108 (2024)
48. S.J. Liu, Y.H. Zhang, R. Sun et al., Multidimensional photopatterning of heterogeneous liquid-crystal superstructures toward higher-level information optics. Adv. Mater. **37**, 2506778 (2025)
49. Z.-Y. Wang, Z. Zhou, H. Zhang et al., Vectorial liquid-crystal holography. eLight **4**, 5 (2024)
50. M. Bass, E. W. V. Stryland, D. R. Williams, W. L. Wolfe, in *Handbook of Optics: Devices Measurements and Properties* (New York: McGraw-Hill Inc., 1995), Ch. 22.
51. N.A. Rubin, Z. Shi, F. Capasso, Polarization in diffractive optics and metasurfaces. Adv. Opt. Photonics **13**, 836–970 (2022)
52. M.S.S. Rahman, J. Li, D. Mengu, Y. Rivenson, A. Ozcan, Ensemble learning of diffractive optical networks. Light Sci. Appl. **10**, 14 (2021)
53. Y. Zuo, B. Li, Y. Zhao et al., All-optical neural network with nonlinear activation functions. Optica **6**, 1132–1137 (2019)
54. I. Bente, S. Taheriniya, F. Lenzini et al., The potential of multidimensional photonic computing. Nat. Rev. Phys. **7**, 439–450 (2025)
55. A. Zaidi, N.A. Rubin, M.L. Meretska et al., Metasurface-enabled single-shot and complete Mueller matrix imaging. Nat. Photonics **18**, 704–712 (2024)
56. Y. Fan, W. Huang, F. Zhu et al., Dispersion-assisted high-dimensional photodetector. Nature **630**, 77–83 (2024)
57. X. Wang, T. Van Mechelen, S. Bharadwaj et al., Exploiting universal nonlocal dispersion in optically active materials for spectro-polarimetric computational imaging. eLight **4**, 22 (2024)
58. Y. Chen, X. Sun, L. Tan et al., All-optical synthesis chip for large-scale intelligent semantic vision generation. Science **390**, 1259–1265 (2025)
59. Z. Xue, T. Zhou, Z. Xu et al., Fully forward mode training for optical neural networks. Nature **632**, 280–286 (2024)